Invited Articles

# Direct numerical simulation of turbulence and microphysics in the Pi Chamber

Theodore MacMillan

Department of Aerospace and Mechanical Engineering, University of Notre Dame, Notre Dame, Indiana, USA

Raymond A. Shaw and Will H. Cantrell

Department Physics, Michigan Technological University, Houghton, Michigan, USA

David H. Richter \*\*

Department of Civil and Environmental Engineering and Earth Sciences, University of Notre Dame, Notre Dame, Indiana, USA

(Received 23 June 2021; accepted 12 January 2022; published 4 February 2022)

The Pi Chamber is a cloud chamber at Michigan Technological University that utilizes moist turbulent Rayleigh-Bénard flow between two temperature-controlled, saturated plates to create cloud conditions in a controlled laboratory setting. This experimental apparatus has been the source of numerous scientific studies but also offers an advantageous platform with which to test numerical modeling approaches. In this study, the primary goal is to use direct numerical simulation (DNS) with Lagrangian aerosol/droplet microphysics to recreate, as realistically as possible, the conditions inside the Pi Chamber. The biggest discrepancies between the DNS and laboratory setups are the Rayleigh number  $(Ra = 7.9 \times 10^6)$  in the DNS) and the use of periodic lateral boundary conditions. Nonetheless, numerical experiments are conducted for two published Pi Chamber cases: steady aerosol injection and the resulting statistically steady-state cloud and transient conditions when aerosol injection is shut off. Generally speaking, the DNS is able to capture many of the salient features observed in the Pi Chamber experiments, both qualitatively and quantitatively, including microphysical details and influences on the fluctuating ambient saturation in the chamber. From the DNS, Lagrangian statistics are interrogated which are otherwise inaccessible from the experimental view. In particular, the supersaturation fluctuations seen by droplets are observed to deviate from a Gaussian distribution—a common assumption in stochastic modeling-and the probability distribution of droplet lifetime does not adhere to the expected behavior assuming solid particles settling in a quiescent medium.

DOI: 10.1103/PhysRevFluids.7.020501

### I. INTRODUCTION

The importance of atmospheric clouds on weather and climate can hardly be overstated, and yet it is widely recognized how difficult it is to study their microphysical details. This is partly due to the multiscale nature of clouds [1,2] but is also, in part, due the difficulties inherent in measuring processes occurring at scales of centimeters to micrometers at distances kilometers above the Earth's surface, while traveling at speeds of approximately 100 m s<sup>-1</sup> (most measurements of clouds are from airplanes). There are also practical difficulties associated with making *in situ* measurements

<sup>\*</sup>David.Richter.26@nd.edu

of inherently transient events such as cloud formation and dissipation. To help combat this, the Pi Chamber (named because of the 3.14-m<sup>3</sup> volume with the cylinder in place) was created at Michigan Technological University to study turbulent cloud properties at the laboratory scale [3]. The key element of the chamber is that cloud conditions can be created and sustained for long time periods (hours) in steady state, which allows for statistical convergence of averages and observation of relatively rare events.

The chamber has been described elsewhere [3]. Here we outline key aspects which are pertinent for the current investigation. Central to the operation of the chamber are temperature-controlled top and bottom surfaces, from which Rayleigh-Bénard flow can be generated. In addition, these upper and lower surfaces can be kept saturated, which, owing to the nonlinearity of the Clausius-Clapeyron relationship, can naturally generate supersaturated conditions (relative humidity exceeding 100%) in the chamber interior. In the context of real clouds, the Pi Chamber temperature gradient is a mechanism for driving a flux of water vapor into the system and can therefore be taken as analogous to the strength of an updraft in the atmosphere (as opposed, for example, to suggesting that there are 10 degree differences of the span of one meter in the atmosphere). The flow in the chamber is turbulent (Ra  $\approx 10^8$ - $10^9$ ), though a large-scale circulation develops as expected [4,5]. This turbulent experimental environment is applicable to better understanding fundamental processes in the atmosphere where a supersaturation (or subsaturation) is created by mixing. For example, in many stratocumulus clouds mixing at the cloud top plays an important role. In cumulus clouds, mixing at cloud edge (entrainment) is thought to be key to the evolution of the cloud droplet size distribution. In either case, fluctuations in the scalar fields (temperature and water vapor concentration) and therefore the saturation ratio and the resulting responses of cloud droplets are of interest. When aerosol particles are injected into the supersaturated chamber at known rates, they serve as cloud condensation nuclei (CCN) on which droplets are formed; the details of this process and the resulting drop size distribution can be studied in unprecedented detail.

In steady-state conditions, the injection of aerosol particles is balanced primarily by droplet removal by settling. Other loss mechanisms of droplets and aerosol particles are of secondary importance [6]. Investigations of stochastic condensation [7,8], relative dispersion [6,9], activation [10,11], cloud glaciation [12], and radiative transfer [13] have been based on the resulting drop size distributions in such conditions.

Experimental limitations, however, are always present, and certain quantities of interest are inaccessible to direct observation. For example, numerical simulations can provide time-resolved, three-dimensional information over the full flow domain, whereas experimental measurements are typically limited to point measurements. For the Pi Chamber specifically, this could potentially mask potential statistical inhomogeneities due to persistent circulation patterns or the effect of boundary layers which cannot be resolved with current instrumentation in the chamber.

More importantly, perhaps, is the ability of a numerical simulation to provide Lagrangian information—something that is not currently possible in the Pi Chamber experiments (or field observations for that matter). The cloud droplet size distribution is a result of the time history of the environment experienced locally by individual droplets: specifically, the fields of temperature and water vapor yield a scalar supersaturation field that determines the growth of cloud droplets and in turn responds to that growth. As a result, there is a great need for establishing Lagrangian models of aerosol activation and growth. For example, Paoli and Shariff [14], Sardina et al. [15], Siewert et al. [16] developed stochastic models in order to explore the broadening of the droplet size distribution (DSD) due to turbulent fluctuations, which requires knowledge of the fluctuating supersaturation field felt by the droplets as they are advected throughout the domain. These recent contributions can be considered extensions of the concept of stochastic condensation, e.g., see Cooper [17] and the discussion and references therein. In this investigation we treat droplets from a Lagrangian point of view while resolving the fluid turbulence, which has been used numerous times to gain insight into droplet dynamics in idealized turbulent flows [18-21]. We consider the full physics of droplet growth, including the possibility of activation and deactivation of aerosols, which is also inherently related to the Lagrangian sampling of the supersaturation field [10,11]. Finally, we note that the droplet removal problem is an underexplored aspect that is fundamental to the water and heat budgets within the convective flow; here also a Lagrangian perspective can provide unique insights.

Finally, it is worth putting this study into context among the previous comparisons to the Pi Chamber. Thomas et al. [22] perform large eddy simulation of the full Pi Chamber domain using the system for atmospheric modeling, including the sidewalls. While much of the discussion was focused on the sidewall treatment, the microphysical evolution, as well as its effects on the humidity and turbulence levels in the air, were found to be similar to the experimental observations. The work of Grabowski [23] focused on comparing a Lagrangian cloud model (LCM) versus a bin microphysical scheme, again seeing general agreement with the experimental observations. Other direct numerical simulation (DNS) studies, such as Saito et al. [24] and Thomas et al. [25], idealize the domain to consider isotropic, homogeneous turbulence, in an effort to focus on the core region of the chamber. An even simpler representation of the chamber dynamics, that of Krueger [26] which does not resolve turbulence but instead analyzes a model for the evolution of the DSD, explores the role of mean supersaturation in defining the DSD. Presently, we perform DNS of the entire Pi Chamber, focusing in particular on the frequency of activation and deactivation, the regimes of supersaturation fluctuation, the transient evolution of cloud cleaning, and the processes controlling the DSD. Computational expenses prevent the full range of turbulent scales to be matched between the DNS and the experiments, but this first attempt at a fully resolved simulation of cloud droplet activation and growth in turbulent Rayleigh-Bénard flow stands to move forward our understanding of turbulence-microphysics interactions in a similar way to other DNS simulations of atmospheric processes [27].

The goal of the present work is to establish a DNS model which aims to capture the salient features of the Pi Chamber as accurately as possible, despite not being able to achieve the Rayleigh number of the experimental flow due to computational expense. We follow the experimental protocols of Chandrakar *et al.* [7] and Chandrakar *et al.* [6], which provide information on steady-state and decaying clouds, respectively. After establishing a comparison of measured quantities between the DNS and the experiments, including droplet number concentrations and DSDs as a function of aerosol injection rate, we use the DNS to calculate quantities which are inaccessible to the observations. This includes lifetime and activation histories of the aerosols, as well as the supersaturation fields they experience during their lifetimes. As will be seen, both of these quantities deviate from their often-assumed forms, suggesting potential differences between turbulent Rayleigh-Bénard flow and idealized isotropic, homogeneous turbulence.

## II. NUMERICAL FRAMEWORK

In this study we employ DNS for the air phase at a reduced Rayleigh number, which explicitly resolves all scales of turbulent motion. These motions are coupled to Lagrangian droplets, using the "superdroplet" or LCM framework developed and used elsewhere [28–30], where a single computational particle represents an ensemble of aerosols/droplets and evolves in a Lagrangian frame of reference according to the local air properties. The computational model used here is the same as that used by Richter *et al.* [31] for studying the evolution of marine fog, except configured to replicate the conditions in the Pi Chamber. Below we provide a brief overview of the model; additional details can be found in Richter *et al.* [31], Park *et al.* [32], or Helgans and Richter [33].

For the air phase, turbulent Rayleigh-Bénard flow is developed in a horizontally periodic domain with solid walls at the top and bottom (see Fig. 1). The top and bottom wall temperature and relative humidities are prescribed as  $T_{\rm top}$ ,  $T_{\rm bot}$  and  $RH_{\rm top}$ ,  $RH_{\rm bot}$ , respectively, while the air velocity is governed by a no-slip condition. Following Chandrakar *et al.* [7] and Chandrakar *et al.* [6], we set  $T_{\rm bot} = 299$  K and  $T_{\rm top} = 280$  K, with  $RH_{\rm bot} = RH_{\rm top} = 100\%$  (i.e., saturated). The numerical setup is similar to that of Park *et al.* [32], except with moist droplet microphysics included.

The domain size is  $[L_x, L_y, L_z] = [2 \text{ m}, 2 \text{ m}, 1 \text{ m}]$ , a similar aspect ratio as the Pi Chamber, although the numerical model is horizontally periodic and thus does not have sidewalls (x and y

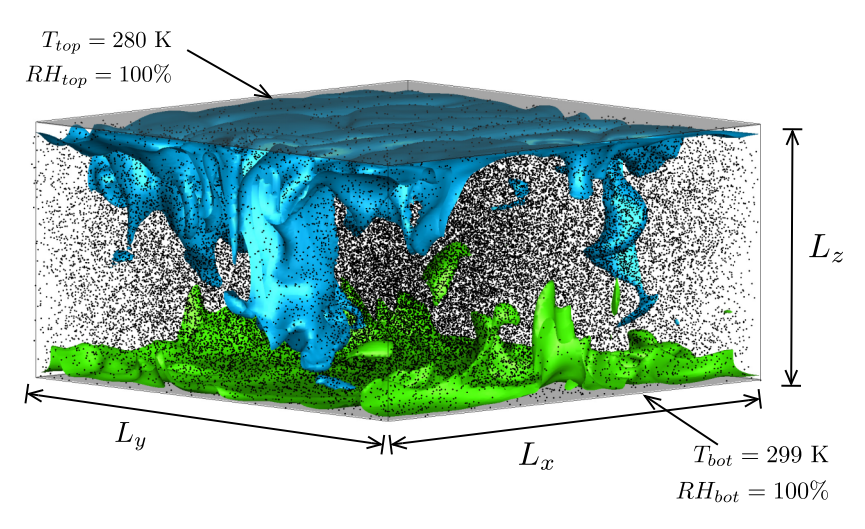


FIG. 1. Representative snapshot of Pi Chamber DNS. Colored isosurfaces are the  $q_v = 12.5 \text{ g kg}^{-1}$  and  $q_v = 17.5 \text{ g kg}^{-1}$  surfaces, and black dots represent the computational droplets.

are the horizontal directions, z is the wall-normal direction). As discussed in detail in Thomas *et al.* [22], without sidewalls the supersaturation levels in the domain interior would approach 20% in the absence of aerosols, and in their presence the droplet growth would be unrealistic. This is due to the fact that in the Pi Chamber, the sidewalls act as a sink of moisture since their temperature is set to be the average temperature of the upper and lower walls, and saturation is not maintained at their surface. To mimic this effect in the present simulations, a volumetric sink term is included in the water vapor conservation equation, whose strength is chosen by meeting a target volume-averaged supersaturation level in the simulation—in this case chosen to be  $SS_{target} = 3.3\%$ , although this could be set to any desired value. Note that this is a different strategy than that of Thomas *et al.* [22] or Grabowski [23], who attempt to represent the sidewalls more directly using a flux model and a penalty relaxation method, respectively.

Thus in the present model, the equations governing mass, momentum, and energy conservation in the air phase under the Boussinesq approximation are as follows:

$$\nabla \cdot \mathbf{u} = 0, \tag{1}$$

$$\frac{\partial \mathbf{u}}{\partial t} + \mathbf{u} \cdot \nabla \mathbf{u} = -\nabla \pi + \hat{\mathbf{k}} \frac{g}{T_0} T_v' + \nu \nabla^2 \mathbf{u} + \mathbf{S}_m, \tag{2}$$

$$\frac{\partial T}{\partial t} + \mathbf{u} \cdot \nabla T = \alpha \nabla^2 T + S_T, \tag{3}$$

$$\frac{\partial q_v}{\partial t} + \mathbf{u} \cdot \nabla q_v = \Gamma \nabla^2 q_v + S_v + S_{\text{side}},\tag{4}$$

where  $\mathbf{u}$  is the fluid velocity vector, T is the temperature,  $q_v$  is the water vapor mixing ratio, and  $\pi$  is a pressure variable which enforces the divergence-free condition of Eq. (1). Buoyancy is driven in the vertical direction  $\hat{\mathbf{k}}$  by the acceleration of gravity g, a reference temperature  $T_0 = 300$  K, and the perturbation to the virtual temperature  $T_v = (1 + 0.61q_v)T$ . The diffusivities of momentum, temperature, and water vapor are v,  $\alpha$ , and  $\Gamma$ , respectively. The terms  $\mathbf{S_m}$ ,  $S_T$ , and  $S_v$  are the sources of momentum, temperature, and vapor due to the droplets, and their full expressions can be found in Richter *et al.* [31]. Note that the buoyancy term in Eq. (2) does not explicitly include the effects of the suspended droplets, as is sometimes done for simplicity [34], since the momentum exchange term  $\mathbf{S}_m$  naturally incorporates this tendency. Finally, the term  $S_{\text{side}}$  in Eq. (4) is the water vapor

source/sink term which, as discussed above, allows us to meet a target mean volume supersaturation in the domain, thus mimicking the effects of the sidewalls in the Pi Chamber.  $S_{\rm side}$  is constant and uniform in time and throughout the volume, and the determiniation of its value is described in detail below. Equations (1)–(4) governing the air phase are solved using a pseudospectral discretization in the horizontal directions, and second-order finite differences in the vertical direction. The  $[L_x, L_y, L_z] = [2 \text{ m}, 2 \text{ m}, 1 \text{ m}]$  domain is discretized using  $[N_x, N_y, N_z] = [128, 128, 128]$  grid points. Time integration is performed using a third-order Runge-Kutta scheme and a constant time step of  $\Delta t = 0.05 \text{ s}$ .

Aerosols and water droplets are tracked from a Lagrangian frame of reference:

$$\frac{d\mathbf{x}_p^i}{dt} = \mathbf{v}_p^i,\tag{5}$$

$$\frac{d\mathbf{v}_{p}^{i}}{dt} = \frac{c_{1}}{\tau_{p}}(\mathbf{u}_{f} - \mathbf{v}_{p}^{i}) - g_{p}\hat{\mathbf{k}},\tag{6}$$

$$\frac{dd^i}{dt} = c_2(q_f - q_*),\tag{7}$$

$$\frac{dT_p^i}{dt} = c_3 \left( T_p^i - T_f \right) + c_4 \frac{dd^i}{dt},\tag{8}$$

where the coefficients  $c_1$ ,  $c_2$ ,  $c_3$ , and  $c_4$  are used to simplify the equations down to their fundamental form. The full equations, which include the droplet and solute material properties, are provided in the Appendix. The droplet equations (5)–(8) are integrated using an implicit, backward Euler scheme with the same  $\Delta t$  as used for the surrounding air. The evolution of the *i*th particle's position  $\mathbf{x}_p^i$ , velocity  $\mathbf{v}_p^i$ , diameter  $d^i$ , and temperature  $T_p^i$  depend on the local fluid velocity  $\mathbf{u}_f$ , humidity  $q_f$ , and temperature  $T_f$  interpolated to the droplet location using sixth-order Lagrange interpolation. The water vapor mixing ratio at the droplet surface,  $q_*$ , is based on Köhler theory, including both droplet curvature and solute effects (a full expression can be found in Richter *et al.* [31] and in the Appendix). Here we consider a solute of pure NaCl, and the aerosols have a critical activation radius and supersaturation of 0.94  $\mu$ m and 0.076%, respectively. The timescale  $\tau_p = \rho_p d^2/18\nu \rho_f$  is the Stokes acceleration timescale, indicating how quickly a droplet with density  $\rho_p$  can be accelerated in a fluid with density  $\rho_f$ .

In addition to these properties, according to the superdroplet framework [29], each particle also has a multiplicity  $\xi^i$  which represents the total number of real droplets represented by the particle. While the code has the capability of representing collision/coalescence, the primary mechanism by which the multiplicity can change, we do not consider this here and thus the multiplicity for an particular particle stays constant throughout the entire simulation. The multiplicities in the current simulations range from 10 at an injection rate of  $\dot{n} = 1 \text{ cm}^{-3} \text{ min}^{-1}$  to 10 000 at an injection rate of  $\dot{n} = 100 \text{ cm}^{-3} \text{ min}^{-1}$ . These choices ensure that there are, on average, at least 3 particles per computational grid cell in all simulations [29]. We have also conducted convergence tests to verify that droplet and supersaturation statistics are robust to this choice of multiplicity (not shown here).

In the Pi Chamber experiments, the dimensionless Rayleigh number  $Ra = g\Delta T L_z^3/(T_0 v\alpha)$  is on the order of  $Ra \sim 10^9$ , where  $\Delta T$  is the difference  $T_{\rm bot} - T_{\rm top}$ . Due to computational constraints, however, the DNS in the current simulations is restricted to  $Ra = 7.9 \times 10^6$ , which is accomplished by setting the gravity felt by the fluid to  $g = 0.043 \, {\rm m \, s^{-2}}$ . This is as opposed to changing the material properties  $\nu$  or  $\alpha$  or the temperature difference  $\Delta T$ , since these parameters are essential for establishing the proper supersaturation levels, thus maintaining the proper interaction between the humidity fields and the suspended droplets (note that other related studies take the former approach of modifying the viscosity, for example Thomas *et al.* [25] and Grabowski and Thomas [35]). With this lower value of Ra, however, we seek to ensure that the dimensionless settling velocity of the droplets matches that of the experiments so that the droplet fall speeds relative to the turbulence strength remains the same. In this regard, we take as a characteristic droplet

settling velocity  $w_s = \tau_p^{1\mu m} g_p$ , which is the Stokes settling velocity of a 1- $\mu$ -diameter droplet in air. As a characteristic fluid velocity scale, we take the buoyancy velocity  $U_{\text{buoy}} = \sqrt{g\Delta T L_z/T_0}$  and hold the ratio  $w_s/U_{\text{buoy}} = 4.4 \times 10^{-5}$  as the same as what it would be in the experimental chamber. This requires setting the gravity felt by droplets to be different than that felt by the flow  $(g_p = 0.65 \text{ m s}^{-2})$  but achieves dynamic similarity between the experiments and DNS in regards to droplet sedimentation. The corresponding free-fall buoyancy timescale  $\tau_{\text{buoy}} = L_z/U_{\text{buoy}}$  is roughly 19 s.

With these flow and droplet parameters, the dissipation rate near the domain centerline is  $\mathcal{O}(10^{-6} \text{ m}^2 \text{ s}^{-3})$ , which corresponds to a droplet Stokes number  $\text{St} = \tau_p/\tau_K = \mathcal{O}(10^{-6})$  where  $\tau_K$ is the centerline Kolmogorov timescale, thus suggesting that droplet dynamics in these simulations are dominated by activation/growth and settling rather than inertial effects. It is worth noting that the grid size required to achieve the experimental value of Ra  $\sim 10^9$  would require upwards of  $\mathcal{O}(1000^3)$  grid points to resolve both the turbulent mixing in the domain interior, as well as the details of the thermal boundary layer at both the top and bottom wall [36]. The primary effect of reducing to Ra =  $7.9 \times 10^6$  is that the large-scale circulation is weaker than it would be in the experimental chamber. Thus the turbulence kinetic energy, and correspondingly the dissipation rate, are much lower (in a dimensional sense) in the DNS than would be expected in the experiments. Accordingly, as noted above, we modify the droplet sedimentation rate so that  $w_s/U_{\text{buoy}}$  matches the experimental values and focus in this study primarily on the microphysical properties since we do not necessarily expect certain turbulence statistics (e.g., spectra) to quantitatively match the experimental values. Instead, the hypothesis here is that the supersaturation fluctuations drive the microphysical processes of interest, and the Rayleigh number is sufficiently high that the droplet and aerosol behavior matches that of the experiments. Indeed, the results shown below suggest that we have generated a fluctuating environment sufficient for recreating observed microphysics and that the details of the turbulence statistics are not as important as the process of droplets responding to realistic supersaturation fluctuations.

Initially, the domain is spun up in the absence of any aerosols or droplets, until the turbulent Rayleigh-Bénard flow reaches a statistically steady state. As this is occurring, the spatially uniform vapor sink  $S_{\text{side}}$  is actively controlled until the desired volume-mean supersaturation  $SS_{\text{target}}$  is achieved. This precursor simulation is performed prior to any of the aerosol simulations reported below, and the resulting constant value of  $S_{\text{side}}$  is tested in an unladen run to ensure that it provides the desired  $SS_{\text{target}}$ . Once this value of  $S_{\text{side}}$  corresponding to  $SS_{\text{target}}$  is determined, it is held constant for all future aerosol loadings since it is meant to represent the assumed-unchanged sidewall sink. For the simulations presented in this work, a value of  $S_{\text{side}} = -2.15 \times 10^{-6} \, (\text{kg/kg}) \, \text{s}^{-1} \, \text{m}^{-3}$  is used.

Once the statistically steady flow has been developed, we inject aerosols in order to reach the steady-state cloud conditions analyzed by Chandrakar  $et\ al.$  [7], and the aerosol injection rate is the primary parameter we vary across the simulations. See Fig. 2 for a demonstration of the adjustment in relative humidity toward a statistically steady state as aerosols are injected at different rates. Lagrangian particles are continually initialized at random locations along the domain centerplane at a specified rate, with monodisperse, dry diameters of  $d^i=100$  nm and uniform hygroscopicites associated with NaCl salt (see Richter  $et\ al.$  [31]); once injected into the chamber, they grow to their hydrated size which is close to 1  $\mu$ m. Since full Köhler physics is considered, the process of activation and condensational growth is naturally handled by the Lagrangian microphysical model—this is in contrast to both Thomas  $et\ al.$  [22] and Grabowski [23], who make approximations as to the process of both injection and activation. In the case of Thomas  $et\ al.$  [22], which uses spectral bin microphysics, injection is mimicked by imposing a droplet number concentration in the domain interior. Grabowski [23], on the other hand, uses a modified Twomey activation scheme where supersaturation fluctuations dictate the number of new, activated droplets to initiate.

From an ensemble of Lagrangian time series of tracers in the unladen flow, multiple timescales can be calculated. First, to describe the quasiperiodic, recirculating trajectories exhibited by

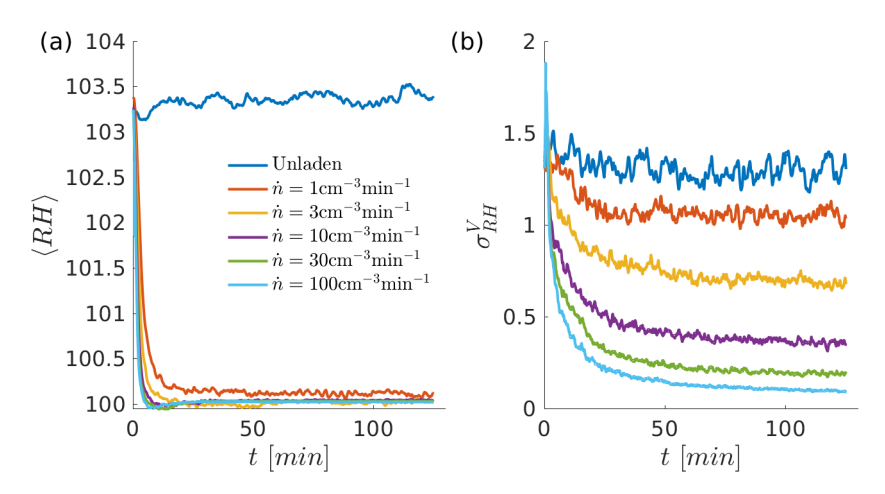


FIG. 2. (a) Volume-averaged relative humidity  $\langle RH \rangle$  and (b) standard deviation  $\sigma_{RH}^V$  of volume-averaged relative humidity as a function of time for all aerosol injection rates.

Rayleigh-Bénard flow, a frequency spectrum is constructed of the Lagrangian vertical velocity time series, and the peak period is calculated to be  $\tau_{\rm recirc} \approx 3.7$  min. This is a characteristic timescale associated with how long it takes a tracer to complete a circuit from one wall to the other and back, and will be used to interpret particle lifetimes in a later section. Second, an integral timescale  $\tau_I$  of the flow is calculated by computing the autocorrelation of the Lagrangian supersaturation seen by tracers in the unladen case. As Table I shows, this can be compared to the cloud or phase relaxation time  $\tau_c = (2\pi \langle n_d \rangle \langle d \rangle \Gamma)^{-1}$  to create a Damköhler number  $Da \equiv \tau_I / \tau_c$ , where the limit of Da > 1 corresponds to systems where inhomogeneous droplet properties can be expected due to their rapid response as compared to the turbulence [20]. From Table I, it is clear that the injection rates considered here begin around  $Da = \mathcal{O}(1)$  and then increase into this inhomogeneous range. Here  $\langle n_d \rangle$  is the mean droplet number concentration after a statistically steady state has been achieved, and  $\langle d \rangle$  is the mean droplet diameter. Throughout this study, volumetric averages over the full domain are denoted with angle brackets  $\langle \cdot \rangle$ , while horizontal averages are denoted with overlines : We also note that much of the subsequent analysis is done in dimensional units, since one primary goal is to compare to specific experimental measurements; however, we recognize the insight gained by considering nondimensional quantities and relate features to the above timescales as appropriate.

TABLE I. Simulation parameters. Ra is the Rayleigh, held the same across the simulations.  $\tau_{\text{buoy}}$  is the free fall buoyancy timescale,  $\tau_{\text{recirc}}$  is a characteristic recirculation timescale calculated by peak of the frequency spectrum of Lagrangian tracers,  $\tau_c$  is the phase relaxation time,  $\tau_I$  is the Lagrangian integral timescale of the flow, calculated from Lagrangian tracer trajectories of supersaturation in the unladen flow, and Da =  $\tau_I/\tau_c$  is the Damköhler number.

Simulation no.	$\dot{n} \; (\mathrm{cm}^{-3}  \mathrm{min}^{-1})$	Ra	$\tau_{\text{buoy}}$ (s)	$\tau_{\text{recirc}}$ (s)	$\tau_c$ (s)	$\tau_I$ (s)	Da
1	0	$7.9 \times 10^{6}$	19	222	_	60	_
2	1	$7.9 \times 10^{6}$	19	222	41	60	1.5
3	3	$7.9 \times 10^{6}$	19	222	14	60	4.3
4	10	$7.9 \times 10^{6}$	19	222	4	60	17
5	30	$7.9 \times 10^{6}$	19	222	1	60	56
6	100	$7.9 \times 10^{6}$	19	222	0.4	60	153

The growth of the droplets, the resulting cloud, as well as the response of the background air flow are monitored until a statistically steady state is achieved for each injection rate. Then, in Sec. III B, we abruptly shut off the constant aerosol injection rate to investigate the transient, cloud-cleaning conditions explored in Chandrakar *et al.* [6]. Table I provides an overview of the simulations considered presently.

#### III. RESULTS

## A. Steady state

## 1. Humidity fluctuations

We begin by characterizing the changes to the relative humidity in the chamber as a result of aerosol injection. Shown in Fig. 2 are time series of the volumetric mean and variance of relative humidity in the domain. As expected, the unladen  $\langle RH \rangle$  fluctuates around the desired 103.3% and also exhibits the highest standard deviation  $\sigma_{RH}^V$ . Once aerosols are introduced, the volume mean  $\langle RH \rangle$  quickly approaches saturation, and Fig. 2(b) shows that the fluctuations in  $\langle RH \rangle$  are suppressed with increasing injection rate. This behavior is similar that observed in the Pi Chamber and reflects the ability of large numbers of aerosol particles to quickly extract excess moisture—otherwise understood as a decrease in the cloud (or phase) relaxation time  $\tau_c$  with increasing aerosol number concentration [20]. As the aerosol injection rate is increased, Fig. 2(b) shows that the volume-based relative humidity fluctuations are suppressed to near-zero at the highest injection rates, and that their temporal variability is diminished as well. It will be shown later that although  $\sigma_{RH}^V$  is small, the fluctuations still facilitate aerosol deactivation/reactivation throughout the droplet lifetimes.

Once at the statistically steady state, defined herein as t > 50 min, Fig. 3 shows the temporally and horizontally averaged profiles of several thermodynamic quantities at the different aerosol injection rates. While the volume-mean relative humidity target is set to  $SS_{target} = 3.3\%$ , Fig. 3(a) shows that the horizontally averaged  $\overline{RH}$  varies considerably with height for the unladen case. With aerosol injection, the mean centerline  $\overline{RH}$  drops close to saturation levels and even below for the case of the lowest injection rates. The presence of subsaturated conditions reflects the combined presence of the sidewall water vapor sink along with an insufficient number of droplets to replenish the water vapor field. At higher injection rates the profile of  $\overline{RH}$  becomes more uniform with height as the fluctuations are systematically reduced at the centerline [Fig. 3(b)].

Near the upper and lower boundaries, peaks of both RH and  $\sigma_{RH}$  are seen and result from the different molecular diffusivities of temperature and water vapor (see the discussion in Chandrakar *et al.* [37]). In turbulent Rayleigh-Bénard flow, these peaks roughly correspond to the upper limit of the boundary layer (approximately 10 cm in the present simulations), and their vertical extent would be expected to decrease with increasing Ra. As already seen in Figs. 2(b) and 3(b) shows that the variance of the relative humidity fluctuations are significantly damped throughout the entire domain, even near the walls. While the presence of aerosols pushes  $\overline{RH}$  toward saturation throughout the entire domain, especially at the highest injection rates, Figs. 3(c) and 3(d) show that these result from somewhat subtle modifications to the temperature and water vapor mixing ratios, in part because the boundary values of these quantities are held fixed in all cases.

Since the fluctuations of supersaturation are critical for developing stochastic models of droplets which can capture realistic evolution of the droplet size distribution [15,17], it is worth examining their statistics in the present calculations. It is shown in Chandrakar *et al.* [7] that the fluctuations of supersaturation in the unladen flow are very nearly Gaussian. This is also commonly implemented in simulations of homogeneous, isotropic turbulence that include droplet growth (e.g., Ref. [24]). It has recently been shown, however, that in Rayleigh-Bénard convection with adiabatic sidewalls the supersaturation distribution is negatively skewed [37,38]. The simulations of Thomas *et al.* [22], meanwhile, see a slight non-Gaussianity, with preference for supersaturation events, presumably due to the influence of unsaturated sidewalls. Here, Fig. 4(a) shows in the solid blue line that the supersaturation fluctuations at the centerplane are slightly non-Gaussian as well, exhibiting a

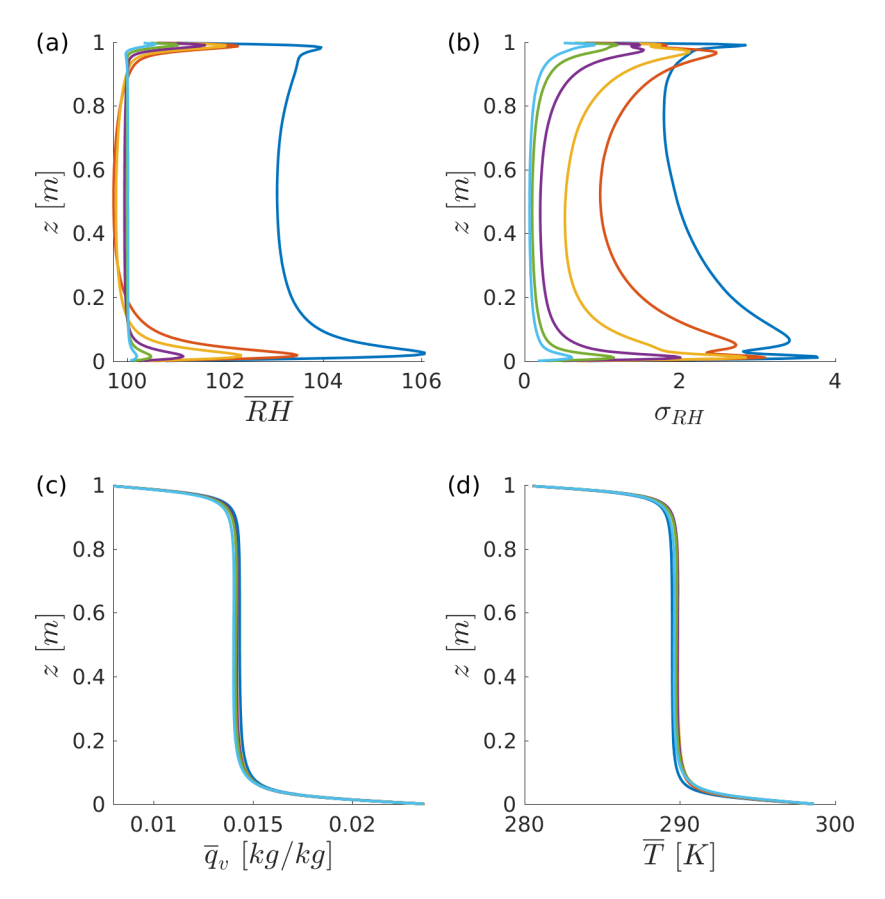


FIG. 3. Temporally and horizontally averaged profiles of (a) relative humidity  $\overline{\text{RH}}$ , (b) its standard deviation  $\sigma_{\text{RH}}$ , (c) water vapor mixing ratio  $\overline{q}_v$ , and (d) temperature  $\overline{T}$  as a function of height across the domain. Line colors are the same as in Fig. 2(a).

modest skewness toward positive supersaturation events. The skewness of the unladen distribution in Fig. 4(a) is 0.54, and the kurtosis is 2.9; the Gaussian fit is plotted in a dashed line. These deviations from a normal distribution highlight potential differences between centerline statistics of Rayleigh-Bénard turbulence and homogeneous isotropic turbulence, but we suspect that these statistics might become more Gaussian with increasing Ra as the turbulence becomes stronger in the interior. When comparing to the PDF provided by Chandrakar *et al.* [7], the small amount of skewness in the experiments appears to be on the subsaturation side, qualitatively opposite to what is seen in the present simulations although the deviations are small.

When aerosols are added, Figs. 4(b)–4(f) demonstrate the narrowing of the s' PDF, as already implied by Figs. 2 and 3. As the injection rate is increased, the tails of the distribution rapidly collapse, and certain non-Gaussian features are enhanced, especially in the tails on the right side of the distributions. These apparent skewnesses indicate that even in the presence of aerosols and cloud droplet growth, it is more likely to have extreme supersaturation fluctuations than it is to have extreme subsaturation fluctuations. In contrast, both the bin and Lagragian microphysics results of Grabowski [23] display significant non-Gaussianity, with heavier tails on the left side of the PDF, although both the injection scheme as well as treatment of activation is quite different in their study.

More interesting, however, is the Lagrangian behavior shown in the circles in Figs. 4(b)-4(f), namely, the PDFs of s', but this time as seen by a large number of particles during their lifetime. In each simulation with aerosol injection, at least  $10^4$  randomly chosen aerosols are tagged at their

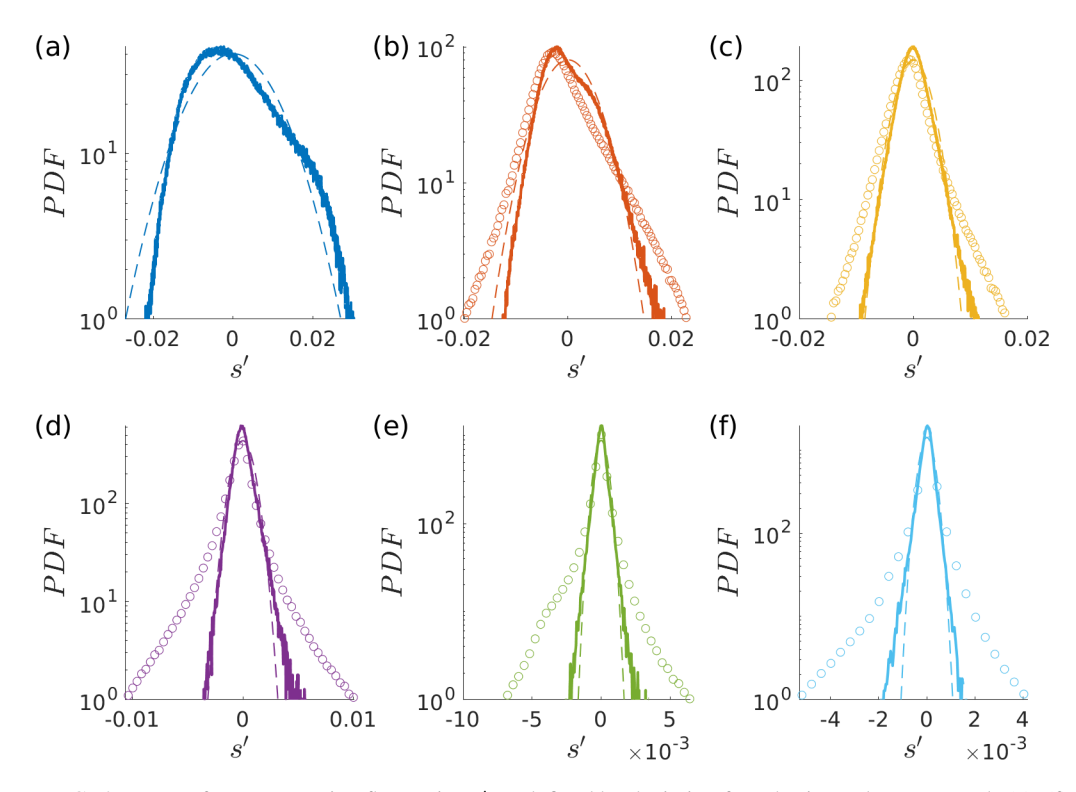


FIG. 4. PDFs of supersaturation fluctuation s', as defined by deviation from horizontal mean. Panels (a)–(f) refer to the increasing injection rates, starting from the unladen case in panel (a). Solid lines: PDF computed from the flow at the domain centerplane at multiple times; dashed lines: Gaussian fit to the centerplane PDF; circles: PDF constructed from the local values of s' taken along at least  $10^4$  droplet trajectories.

initiation, and they output their properties (e.g., position, radius, temperature, ambient conditions, etc.) at an interval of 0.5 s throughout their entire lifetime, including both activated and unactivated states. From these full trajectories, the distribution shown in Fig. 4 is constructed by taking all values of s' experienced by these particles along their trajectories, where s' is defined by the local fluctuation of supersaturation from the horizontal mean at that height.

What is striking when comparing the solid lines and circle markers in Figs. 4(b)–4(f) is the emergence of heavy tails in the Lagrangian PDFs, revealing potentially large fluctuations of both sub- and supersaturation when tracking individual droplets. These Lagrangian PDFs are clearly non-Gaussian, and this observation has strong implications for the development of stochastic droplet growth models, since those by for example Sardina *et al.* [15], Chandrakar *et al.* [7], Desai *et al.* [8], and Saito *et al.* [24] (among others) assume Gaussian supersaturation statistics. The degree to which this non-Gaussian behavior is a function of Rayleigh number and the sidewall treatment (i.e., the volumetric water vapor loss term) is unclear but nonetheless highlights the potential differences between homogeneous isotropic turbulence and turbulent Rayleigh-Bénard flow.

## 2. Droplet properties

For the steady-state cloud cases, aerosols are continuously injected until various statistics, including the DSD, achieve stationarity. This state would also imply that a balance is found between aerosol injection and aerosol/droplet removal, either through gravitational sedimentation or deposition to the sidewalls. In the present simulations, the only removal mechanism is through

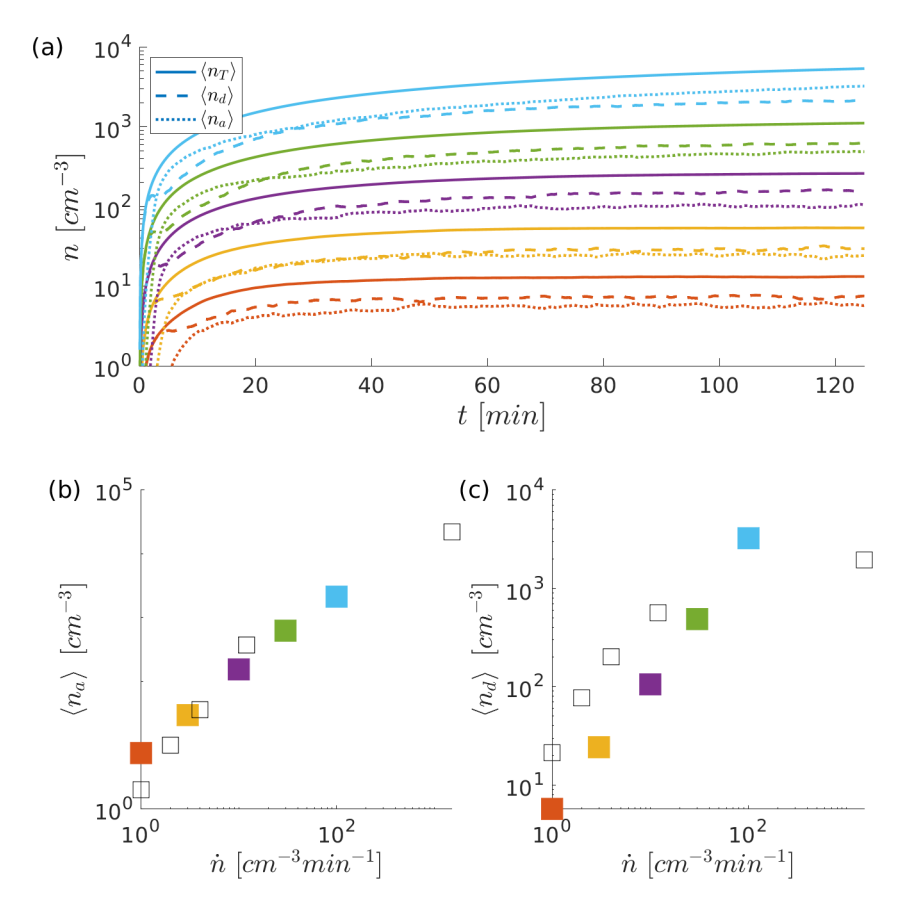


FIG. 5. (a) Time series of number concentrations of aerosols (dotted), droplets (dashed), and total (solid), as defined by the activation state. (b) Steady-state aerosol number concentration  $n_a$  as a function of injection rate. For the highest two aerosol injection rates,  $n_a$  is the last recorded value. (c) Steady-state droplet number concentration  $n_d$  as a function of injection rate. Hollow symbols are from Chandrakar *et al.* [7], and colors refer to aerosol injection rates [see legend of Fig. 4(b)].

deposition to the lower boundary, so it is expected that aerosol numbers may be larger than in the experiments.

To test this, Fig. 5(a) contains time series for the droplet, aerosol, and total (droplet + aerosol) number concentrations from the time when aerosol injection begins, as defined by their activation state (radius larger than the critical radius). For the lower injection rates considered, the total number concentration approaches a constant value, with the number of droplets exceeding that of the aerosols. This indicates that a steady balance has been reached between aerosol injection, aerosol activation, and droplet sedimentation out of the domain.

For the highest aerosol injection rate, however, the total droplet number concentration approaches a relatively constant value after  $\approx$ 60 min, but the aerosol number concentration continues to rise, even in exceedance of the number of droplets. Since the aerosols essentially have no other removal mechanism except through activation, their population builds up, and owing to their very low settling velocity, this increase in aerosol number would likely continue for a very long time. See for example the discussion in Thomas *et al.* [22]. Another way of describing this behavior is by referring to the activation fraction of the chamber, defined by the ratio of the number of activated droplets to the total. In the limit of very low injection rate, one would expect an activation of 1—i.e., all aerosols activate. As the injection rate increases, Shawon *et al.* [10] show clearly that the activation fraction

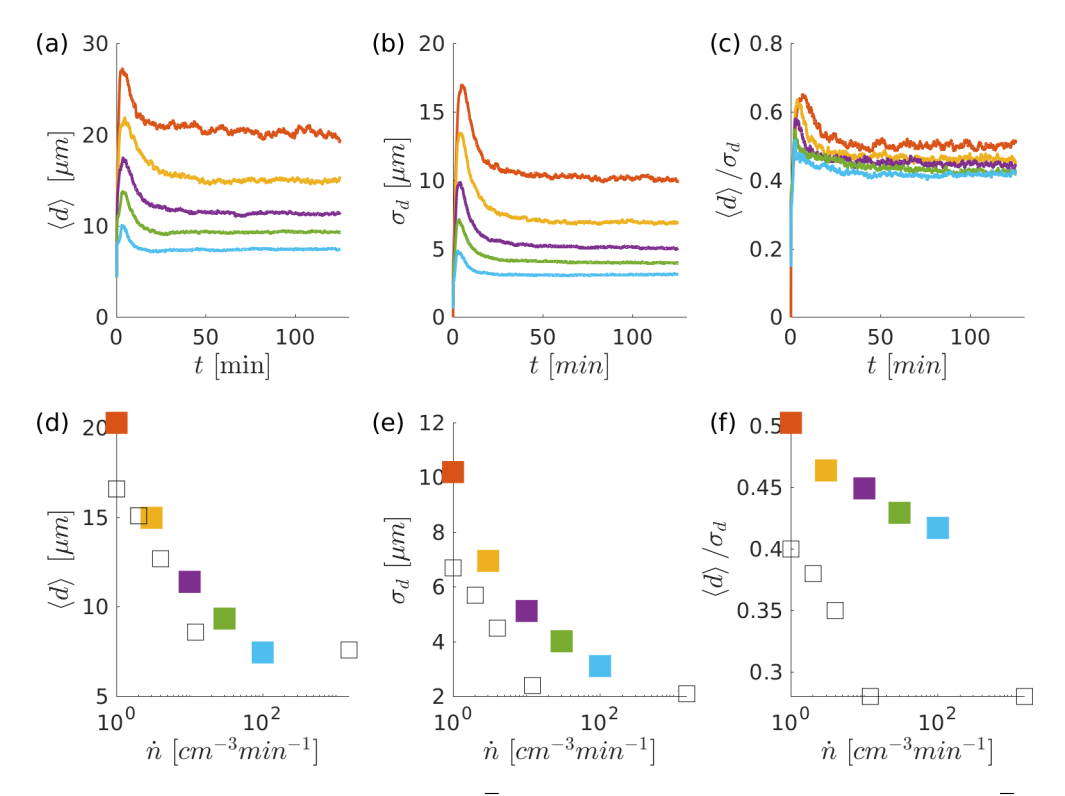


FIG. 6. [(a)–(c)] The droplet mean diameter  $\overline{d}$ , standard deviation  $\sigma_d$ , and relative dispersion  $\sigma_d/\overline{d}$  as a function of time for the various injection rates. [(d)–(f)] The steady-state  $\overline{d}$ ,  $\sigma_d$ , and  $\sigma_d/\overline{d}$  versus  $\dot{n}$ . Hollow symbols are the experimental measurements from Chandrakar *et al.* [7].

decreases in the Pi Chamber, down to roughly 0.5 at their highest injection rate. In the current simulations, as can be seen in Fig. 5, the activation fraction transitions from above 0.5 to a minimum of 0.4 for the highest injection rate. This reduction with injection rate is qualitatively similar to the experimental findings, but the complex interplay between aerosol injection and mean/fluctuating supersaturation has yet to be fully understood [10,11].

Figures 5(b) and 5(c) plot the steady-state number concentration of aerosols ( $\langle n_a \rangle$ ) and droplets ( $\langle n_d \rangle$ ), respectively, against the aerosol injection rate (we take the final value of aerosol number concentration for the highest injection rate since it is still increasing). Also included in this figure are the measured values from Chandrakar *et al.* [7] (hollow symbols). The aerosol number concentrations are in good agreement with the measurements, while the droplet number concentrations are mostly less than the experimental values. A levelling-off of the droplet number concentration is seen in the experiments which is not observed in the simulations, likely due to the absence of any removal mechanism other than sedimentation to the lower wall. Another possible explanation is that in the experiments, small droplets go undetected if they fall below the  $d \approx 7 \ \mu m$  threshold of the phase Doppler interferometer instrumentation [9].

While Fig. 5 illustrates the aerosol and droplet populations approaching a steady state, Fig. 6 provides information about the stationarity of the droplet size statistics. Figures 6(a)-6(c) show the evolution of the mean droplet diameter  $\langle d \rangle$ , the droplet standard deviation  $\sigma_d$ , and the relative dispersion  $\sigma_d/\langle d \rangle$  as a function of time for all injection rates. Only droplets which are activated are included in these statistics, to be consistent with Chandrakar *et al.* [7]. Immediately after the initiation of aerosol injection at t=0, both  $\langle d \rangle$  and  $\sigma_d$  overshoot their equilibrium value for all injection rates, achieving statistically steady values around  $t\approx 40$  min. In preliminary experiments,

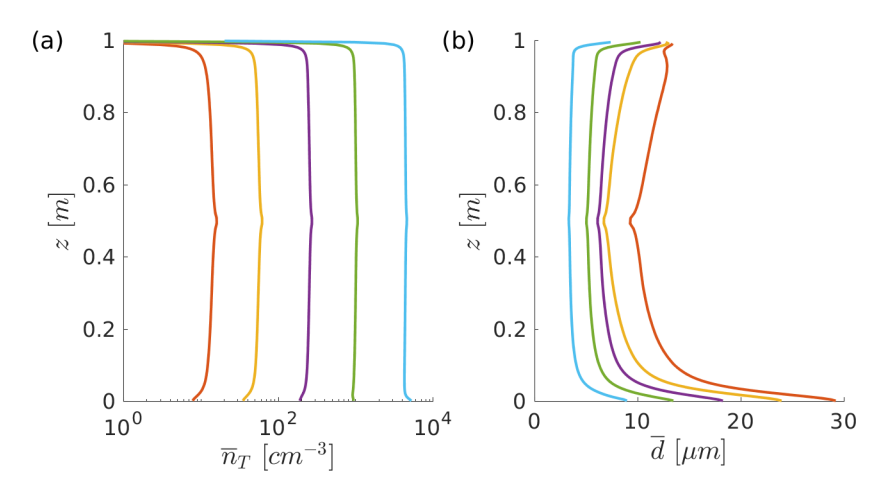


FIG. 7. (a) Total number concentration  $\bar{n}_T$  (droplets and aerosols), horizontally and temporally averaged, as a function of height; (b) temporal and horizontal mean diameter as a function of height.

this time to achieve stationarity decreases with Ra. For the highest aerosol injection rates, the time series of both  $\langle d \rangle$  and  $\sigma_d$  exhibit clear stationarity, despite the fact that the aerosol and to some degree the droplet number concentrations continue to rise [cf. Fig. 5(a)]. Equilibrium of the droplet size statistics are related to the phase relaxation time  $\tau_c$  of the droplet collection, which in the current simulation setup is a much shorter timescale than that associated with establishing a balance between aerosol injection, activation, and gravitational sedimentation.

Figures 6(d)–6(f) then show the steady-state values of  $\langle d \rangle$ ,  $\sigma_d$ , and  $\sigma_d/\langle d \rangle$  as a function of the aerosol injection rate, compared to the experimental results of Chandrakar *et al.* [7]. While the average droplet size is close in value to the experimental measurements, the standard deviation of diameter is overpredicted in the current simulations, causing an overprediction of the relative dispersion as well. While the values of  $\sigma_d$  seen in the simulations of Thomas *et al.* [22] and Grabowski [23] were similar to those of Chandrakar *et al.* [7], the relative dispersions of both were also much higher than the current results and Chandrakar *et al.* [7], owing to an underestimate of the mean droplet diameter. In the current case, the mean droplet diameter is similar to the experimental values, and the overprediction of  $\sigma_d$  may be caused by differences in the supersaturation fluctuations, which we expect to be a function of Ra [37].

Another factor to consider when interpreting not only the current simulation results but also the experimental measurements is the heterogeneity of droplet statistics. Grabowski [23] comments on the potential of having differences in the DSD at different horizontal locations at a given time, but Fig. 7 highlights that even the mean properties vary with wall-normal location in the chamber.

Figure 7(a) shows that the total number concentration  $\bar{n}_T$ , containing both aerosols and droplets, peaks in the domain interior, decreasing near both boundaries. The exception to this is for the highest two injection rates, where a slight increase in number concentration is found near the lowest boundary, resulting from smaller droplet sizes which inhibit their gravitational sedimentation out of the domain. Figure 7(b) then shows the corresponding mean droplet diameter as a function of height, having a minimum in the domain center where RH is lowest. Near the lower boundary, where peaks of RH are found (cf. Fig. 3), the droplet sizes are significantly larger than in the domain interior. To a certain extent this behavior is expected, since aerosols are injected at the centerline and those which activate would rapidly settle downwards. Furthermore, the mean relative humidity near both boundaries is larger than the interior (cf. Fig. 3), leading to a larger mean diameters in those locations relative to the center. As noted above, this effect is expected to decrease with increasing Ra since the spatial extent of the boundary layer would shrink, but in the present simulations it results in nearly all droplets increasing in size just before sedimenting, hastening the process.

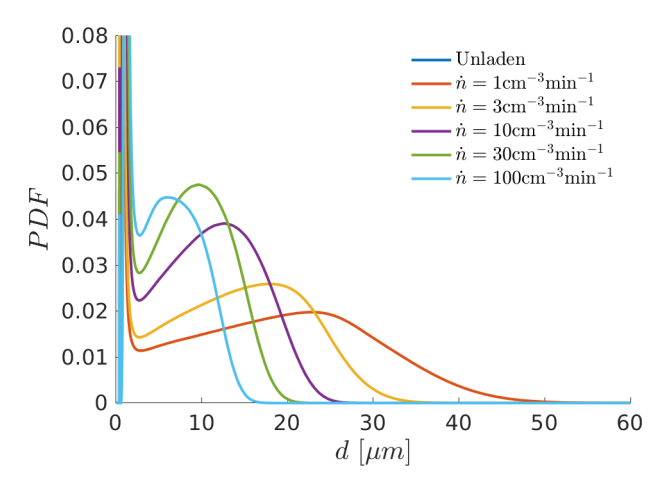


FIG. 8. Droplet size distributions for all injection rates. The large spike centered at  $d < 1 \mu m$  represents unactivated aerosols.

Figure 8 shows the steady-state DSDs for each of the injection rates and is meant to be compared to Fig. 2 of Chandrakar *et al.* [7]. Qualitatively, we see the spectral broadening process identified by Chandrakar *et al.* [7], where a decrease in  $\dot{n}$  leads to a widening of the DSD. A similar broadening of the DSD is also seen in the DNS of Saito *et al.* [24], although their DNS setup is considerably different (homogeneous, isotropic turbulence with a prescribed droplet lifetime). It is also seen in the model simulations of Grabowski [23].

For the lowest injection rate, the current simulations predict a wider distribution than the experiments, already noted above regarding the values of  $\sigma_d$ , while the peak generally compares well to the experiments (again, this is consistent with the favorable comparison of  $\langle d \rangle$ , discussed above). Since the Lagrangian framework resolves the aerosol activation process, there is a sharp peak for all cases which lies below 1  $\mu$ m, reflecting the unactivated aerosols in the system. The trough of the DSDs reflects the critical diameter, which is roughly 1.5  $\mu$ m for all cases.

The true value, however, of the Lagrangian microphysical approach to simulating the Pi Chamber lies in the numerous quantities which can be measured that are experimentally inaccessible. Of particular importance is the distribution of droplet lifetime, which in stochastic models must be specified (e.g., Saito *et al.* [24]) and can play a major role in determining the DSD shape [26]. As such, Fig. 9 presents four important distributions related to the lifetime of the droplets. First, Fig. 9(a) shows the PDF of total lifetime,  $\tau_l$ , from the moment of aerosol injection until its settling out at the lower boundary, regardless of its activation state. In the range of short lifetimes ( $\tau_l \lesssim 5$  min), there is a notable oscillation of the PDF with residence time, which will be explained below.

With increasing injection rate, consistent with the reduction in  $\langle d \rangle$  and a narrowing of the DSD seen previously, the PDF of total lifetime in Fig. 9(a) broadens significantly. A non-negligible number of aerosols injected in the  $\dot{n}=100~\rm min^{-1}cm^{-3}$  can live in excess of an hour (i.e., many timescales  $\tau_I$ ,  $\tau_{\rm buoy}$ , or  $\tau_{\rm recirc}$ ). From Fig. 9(a) we observe that aerosols routinely have lifetimes on the order of tens of minutes, which is generally on the same order of simple estimates based on the time it takes a droplet to settle through the domain through quiescent air at the Stokes terminal velocity  $w_s = \tau_p g_p$ . This timescale,  $\tau_{\rm Stokes} \equiv L_z/w_s$ , would scale as  $d^{-2}$  assuming solid particles (i.e., no condensation/evaporation) and no turbulence, and a droplet of  $d=10~\mu m$  corresponds to  $\tau_{\rm Stokes} \approx 7~\rm min$  using the values prescribed in the DNS (recall in particular the modified value of  $g_p$  used in the DNS). This indicates that a water droplet of this size, which is not changing in size, would take roughly 7 min to settle in a completely still air environment over a distance of  $L_z=1~m$ .

Corresponding to the distribution of  $\tau_l$  in Figs. 9(a) and 10(a) plots the mean of these distributions  $\langle \tau_l \rangle$  as a function of the mean droplet diameter  $\langle d \rangle$  for each of the injection rates. In the dotted black

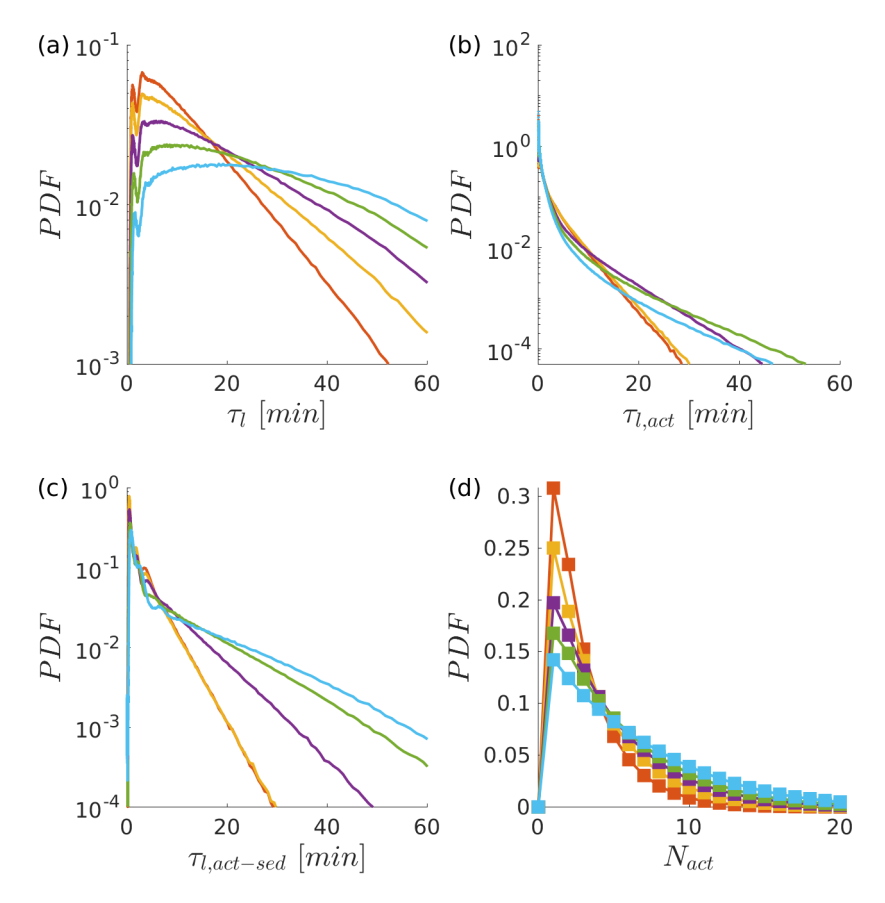


FIG. 9. (a) PDF of total aerosol residence time  $\tau_l$ , from injection until removal from the domain; (b) PDF of activation times  $\tau_{l,\text{act}}$ , from when a droplet is first activated to when it either deactivates or is removed from the domain; (c) PDF only of times between activation and removal  $\tau_{l,\text{act-sed}}$ ; (d) PDF of  $N_{\text{act}}$ , the number of times aerosols have been activated during their lifetime in the domain.

line, Fig. 10(a) also shows the estimate provided by  $\tau_{\text{Stokes}}$ . While the estimate of  $\tau_{\text{Stokes}}$  provides values on the same order of the true mean lifetimes  $\langle \tau_l \rangle$ , two important features must be emphasized. First, the combination of turbulence and droplet growth lead to a distribution that is in reality very wide [cf. Fig. 9(a)], suggesting that caution is required when prescribing a single value of either  $\langle d \rangle$  or  $\langle \tau_l \rangle$  for a given injection rate. Furthermore, the mean lifetime does not scale as  $d^{-2}$  as predicted by  $\tau_{\text{Stokes}}$  but instead appears to be inversely proportional.

To further understand this, Fig. 9(b) presents instead the PDF of times during which the droplets remain activated. This accounts for the fact that droplets in the DNS system routinely deactivate and reactivate and thus would complicate the prescription of a single settling time (or characteristic size) to their entire lifetime. In Fig. 9(b), we see that the tails of this distribution are nearly exponential, with many "activation lifetimes" being less than the total duration of  $\langle \tau_l \rangle$ . This is made clear by Fig. 9(d), which shows the distribution of the number of times an aerosol is activated during its lifetime. Even for the low injection rates, there is a non-negligible chance of being reactivated upwards of 10 times. The mode of this distribution is indeed unity, but it is not uncommon to have droplets deactivating and reactivating multiple times during their lifetimes, especially at the higher injection rates. In the atmosphere, this can have profound effects on the CCN distributions as aerosols are cycled through nonprecipitating clouds [39,40].

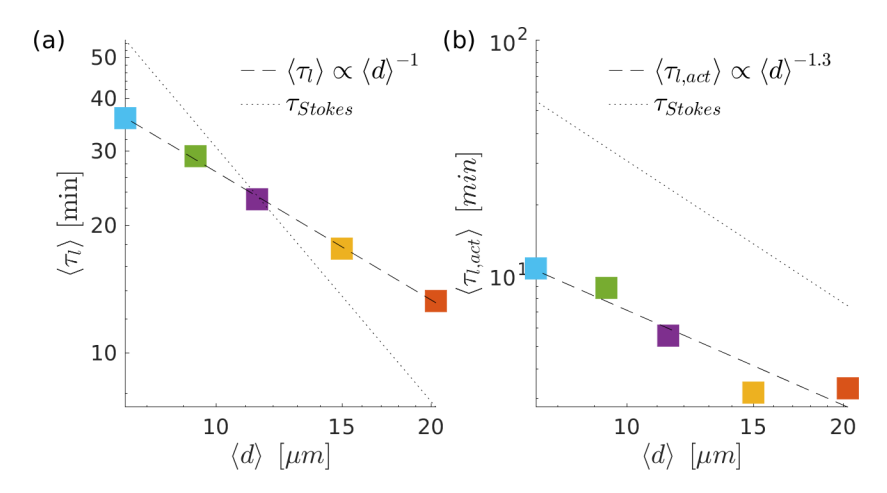


FIG. 10. (a) Mean droplet lifetime  $\langle \tau_l \rangle$  as a function of mean droplet diameter  $\langle d \rangle$  for each of the injection rates  $\dot{n}$ . (b) Same, but for the time from activation until removal. The dashed black line is a power-law fit  $\langle \tau_l \rangle \propto \langle d \rangle^{\lambda}$  for a fitted value of  $\lambda$  given in the legends, and the dotted black line is the estimate given by  $\tau_{\text{Stokes}}$  for each droplet diameter.

Since many of the theories of stochastic condensation do not attempt to account for reactivation processes, Fig. 9(c) shows the PDF of times between droplet activation and gravitational sedimentation, only for those intervals which are not interrupted by deactivation. Here again we see a substantially different distribution from the total lifetime in Fig. 9(a), with exponential tails and times which are shorter than  $\langle \tau_l \rangle$ . Then, Fig. 10(b) shows the same relationship as Fig. 10(a) but between the mean lifetime between activation and removal and the mean droplet diameter. Here, we see a slight increase in the slope, with a fitted relationship going as  $\overline{d}_p^{-1.3}$ , but now the values are substantially lower than the prediction given by  $\tau_{\text{Stokes}}$ . The gravitational settling efficiency, and in particular this depends on droplet growth and boundary layer thickness (i.e., Ra) are important topics which continue to be studied.

Finally, we comment on the shape of the  $\tau_l$  distribution at low residence times and highlight the importance of a Lagrangian interpretation. Figure 11 shows the  $\tau_l$  PDF for the  $\dot{n}=1~{\rm cm^{-3}\,min^{-1}}$  case but shows typical trajectories for certain positions along the distribution. On the left side of the distribution, a peak emerges around  $\tau_l\approx 1~{\rm min}$ . This is followed by a trough and another peak to the right ( $\tau_l\approx 3~{\rm min}$ ), beyond which an exponential distribution is established. This nonmonotonic distribution of  $\tau_l$  is directly linked to the dynamics within the chamber. For the leftmost peak, we plot trajectories of aerosols/droplets which only live between 0.8 and 1.2 minutes. Plotted are time series of height (top), ambient RH (middle), and diameter d (bottom) for a randomly chosen subset of trajectories which fall into this range of lifetimes. What is clear is that the droplets in this range, which begin at the domain midplane, are those which are immediately driven to the lower surface via turbulent downdrafts. Some of these droplets activate and grow immediately, while others do so at a delayed time, but all are pushed to the lower surface within a minute of initiation.

For the second peak (and the maximum of the entire distribution), this is seen to be resulting from a large number of droplets who instead are pushed upwards immediately on initiation. These spend some time near the upper boundary before they are forced downwards by convective motions. This peak of 3 min is quite close to the timescale  $\tau_{\text{recirc}}$ , since this scale describes the time taken by a tracer to recirculate through the flow. Beyond this global maximum in the  $\tau_l$  distribution, the exponential distribution of total residence times is resulting simply from a varying number of excursions from the bottom to the top as aerosols/droplets ride the convective motions associated with Rayleigh-Bénard turbulence—a potential strategy for developing stochastic models. Fitting an exponential to this portion of the distribution provides a characteristic timescale of  $\sim 10$  min, which

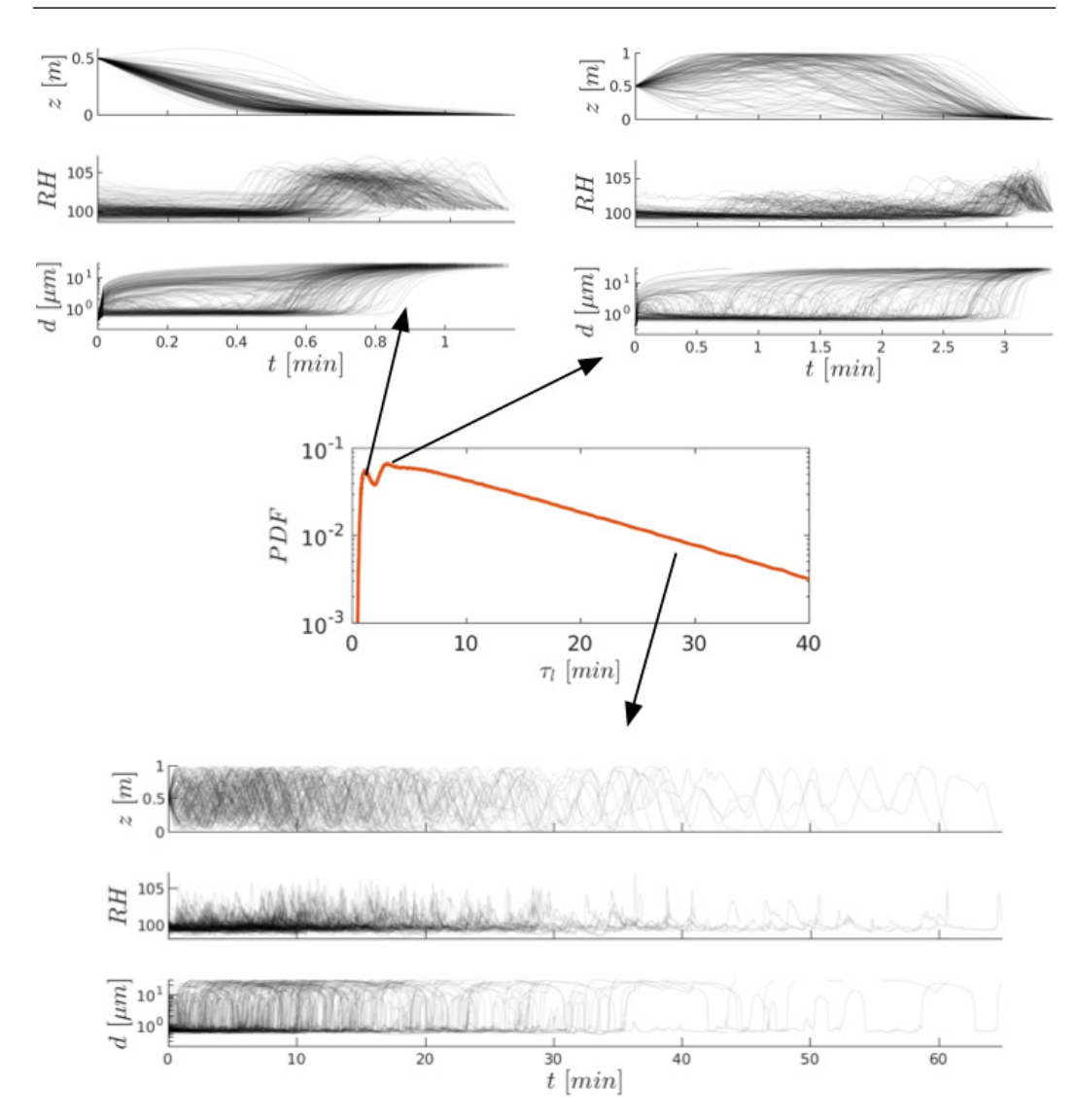


FIG. 11. In the center is the PDF of total lifetime  $\tau_l$  for the  $\dot{n}=1~\rm cm^{-3}\,min^{-1}$  case from Fig. 9(a). For each of the three lifetime ranges indicated by the arrows, sample trajectories are given showing the droplet height, local relative humidity, and diameter. The nonmonotonic PDF of  $\tau_l$  at small lifetimes is clearly due to the periodic circulations which exist in Rayleigh-Bénard turbulence.

is similar to the mean of the distribution and is larger than the characteristic flow scales  $\tau_{buoy}$  and  $\tau_{recirc}$ . The supersaturation experienced by the aerosols is indeed highly variable, while its lifetime is dictated by whether it falls into the boundary layer when nearing the lower surface. Inside this layer, as shown in Fig. 3, the high values of RH near the lower surface cause droplets to universally grow, hastening their removal process.

## B. Transient

Following Chandrakar *et al.* [6], we now briefly examine the transient response of the turbulent cloud to a sudden cessation of aerosol injection. This is done for all injection rates presented in

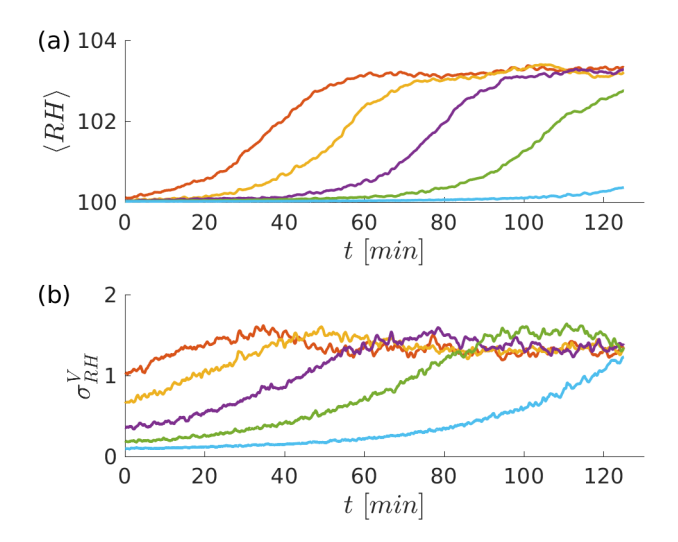


FIG. 12. Transient response of (a) the volume-mean RH and (b) relative humidity variance  $\sigma_{RH}^2$  as a function of time after stopping aerosol injection.

the previous section by stopping the aerosol injection at t = 125 min and running the simulations for an additional 125 min. This transient "cleaning" is important for understanding cloud collapse, rain formation, and pollution scavenging, and in particular we seek to observe the acceleration of this process as aerosols (and therefore competition for excess moisture) become scarce, as seen in Chandrakar *et al.* [6].

Figure 12 shows the response of the chamber humidity as it adjusts to stopping the aerosol injection. Both the mean  $[\langle RH \rangle; Fig. 12(a)]$  and fluctuating  $[\sigma_{RH}^V; Fig. 12(b)]$  relative humidity approach the unladen values, and the response of  $\sigma_{RH}^V$  appears to be underdamped, exhibiting an overshoot before approaching the equilibrium value. More dramatically, the timing of when the approach to equilibrium occurs is strongly dependent on the preceding injection rate. The reason for this is the same as that observed in Chandrakar *et al.* [6]: At the higher injection rates, a large reservoir of unactivated, interstitial aerosols builds up [see Fig. 5(a)], and this takes an increasingly long time to deplete. The size of this unactivated reservoir is related to the activation fraction, which, as argued above and in Shawon *et al.* [10], is a strong function of the level of supersaturation fluctuations. Furthermore, the timing of the increase in RH back to unladen conditions is directly related to the number concentration of interstitial aerosols, which as shown in Fig. 5(b) are close to the experimental values.

Figure 13 shows the corresponding time series of various droplet statistics during the same time intervals. In Fig. 13(a), the depletion of both aerosols and droplets, and how this varies with the preceding injection rate, is evident. The primary mechanism for aerosol removal in the current simulations is activation, since there are no sidewalls to deposit onto and since settling is negligible owing to the low gravitational settling speed. Figure 13(a) demonstrates this, in that at late times the droplet number concentration  $\langle n_d \rangle$  approaches the total  $\langle n_T \rangle$ . As the droplet number concentration falls, Fig. 13(b) then shows the corresponding value of Da as it changes in time based on the current values of  $\langle n_d \rangle$  and  $\langle d \rangle$ . Each case begins above the Da = 1 threshold, indicating a fast cloud droplet response as compared to the turbulence but eventually transition to a slow droplet response regime as time goes on. Similarly to Chandrakar *et al.* [6], as time evolves, the droplet number concentration decreases with a corresponding rise in the mean droplet diameter.

Figures 13(c) and 13(d) show the mean droplet diameter and standard deviation of droplet diameter, respectively, and in both cases the accelerating cloud collapse is associated with a rise in both the mean and fluctuation of droplet diameter. The sharp acceleration is consistent with the

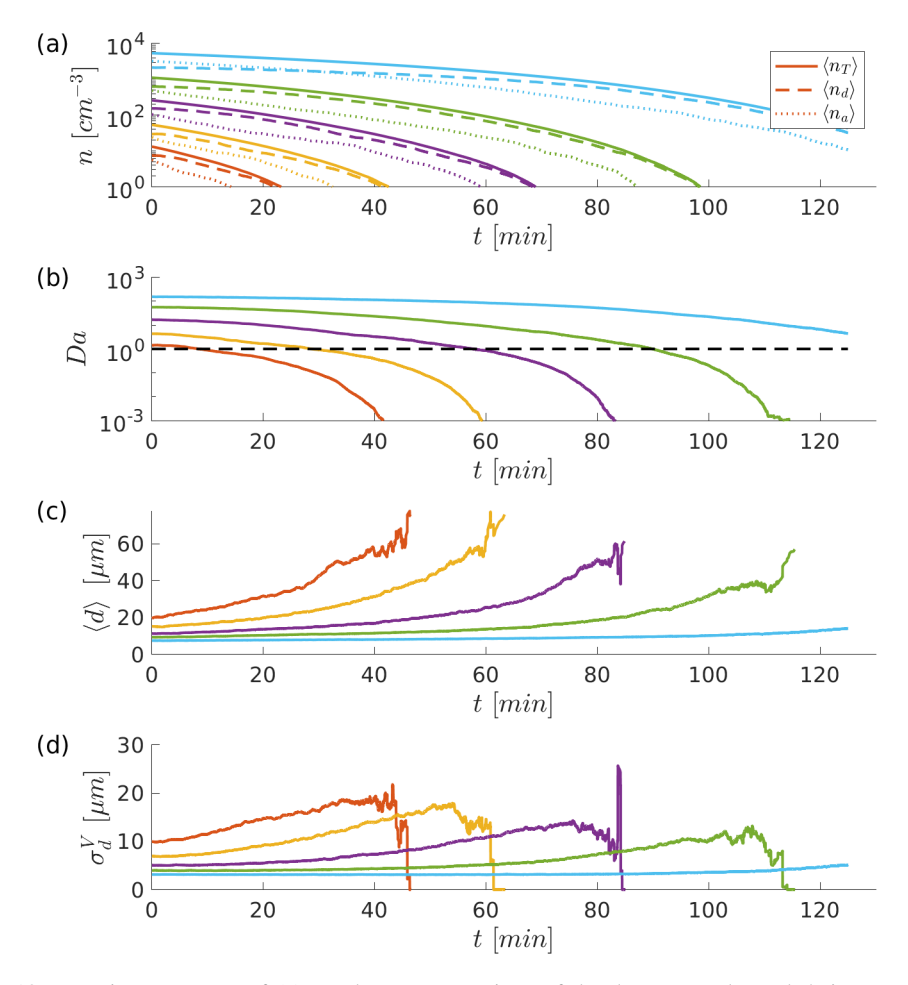


FIG. 13. Transient response of (a) number concentrations of droplets, aerosols, and their sum. (b) The transient Damköhler number Da based on the current droplet number density and mean radius (dashed line is Da = 1); (c) mean droplet diameter; and (d) standard deviation of droplet diameter  $\sigma_d$ , as a function of time after stopping aerosol injection.

crossing of the Da = 1 threshold, as the system adjusts from fast to slow microphysics relative to the turbulence. The behavior of  $\langle d \rangle$  and  $\sigma_d^V$  is seen in Chang *et al.* [3] and Chandrakar *et al.* [6] and is explained by the decrease of competition for excess moisture. For some time interval which depends on the built-up reservoir of aerosols, the droplet diameter and standard deviation remain constant in time as the activation and settling processes remain in equilibrium. However, as fewer and fewer aerosols are available for activation, the remaining droplets grow larger owing to the reduced competition.

Finally, Fig. 14 provides the evolution of the full DSD in the transient cases, where the rise in both  $\langle d \rangle$  and  $\sigma_d^V$  are clear. The general features of these DSD evolutions are similar to those observed by Chang *et al.* [3] and show a clear widening of the DSD with time as the aerosols are depleted. For the lowest preceding injection rate, droplets are seen to grow to nearly 100  $\mu$ m in size toward the end of the cloud, although this likely exaggerated due to the large supersaturation fluctuations present in the system at late times. With larger reservoirs of interstitial aerosols, the evolution of the DSD is both quantitatively and qualitatively similar to Fig. 10 of Chang *et al.* [3], although with different timing owing to the differing amounts of built-up aerosols.

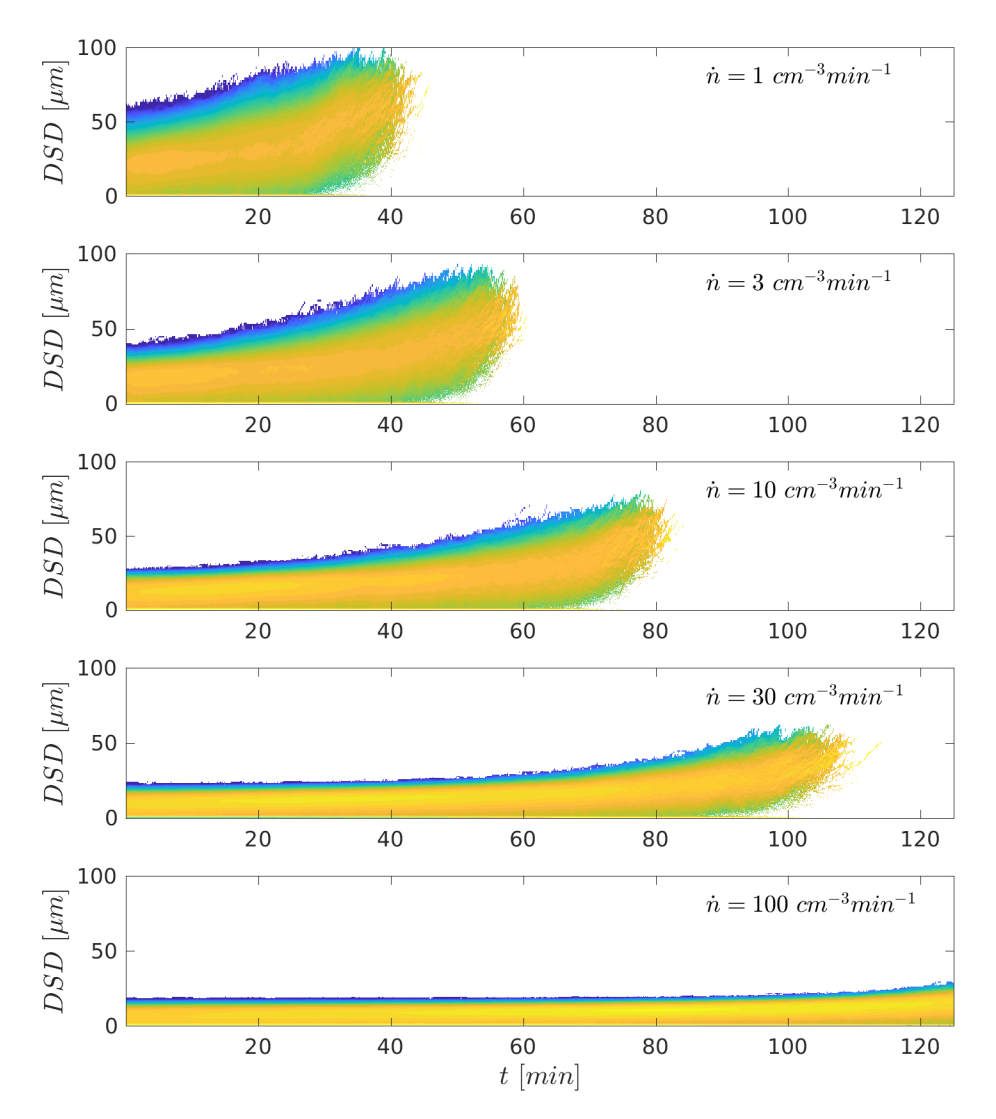


FIG. 14. The cloud DSD as a function of time for each of the transient cases. Colors represent the logarithm of the probability and range between -5 to -1. The color scale is the same in all panels.

## IV. CONCLUSIONS

This work seeks to use DNS to simulate recent Pi Chamber experiments as closely as possible in order to shed light on processes and statistics which are unavailable to laboratory measurements. The simulations are performed at a Rayleigh number of  $7.9 \times 10^6$ , which is significantly lower than the experimental value, and employ periodic lateral boundary conditions instead of solid walls (the dimensionless settling velocity of the droplets are chosen to match experimental conditions). Despite these differences, and the subtleties associated with mimicking water vapor removal at the wall [22], salient features of the DSD, aerosol, and water vapor statistics are well reproduced by the DNS. Certain qualitative features, such as the relationship between aerosol injection rate and activation fraction, match those seen in experiments as well [10].

From this standpoint, several features are observed which extend our understanding of droplet dynamics in the turbulent Rayleigh-Bénard flow. First, the supersaturation fluctuations seen by the

droplets, from a Lagrangian point of view, are not necessarily the same as those measured from a stationary probe and appear to have heavy, non-Gaussian tails. This has strong implications on developing accurate stochastic models of cloud droplet microphysics, since it is the Lagrangian quantity that is required. In particular, vertical gradients of mean supersaturation are strong near the walls of the chamber, although the region where this is expected to influence bulk droplet behavior would reduce with increasing Rayleigh number. In the domain interior, many of the relevant environmental quantities are uniform, but perhaps non-Gaussian.

Another Lagrangian quantity observed in the DNS are the aerosol/droplet lifetimes. Somewhat unexpectedly, aerosols can undergo upwards of O(10) activation/deactivation cycles during their lifetime, confusing the notion of a single lifetime which can be used in models [24,26]. Furthermore, the scaling of mean droplet lifetime with mean droplet size does not behave as  $\langle \tau_l \rangle \sim \langle d \rangle^{-2}$  as often assumed; we instead find an inversely proportional relationship. How this relationship behaves with Ra, and whether it is a fair assessment to take the mean lifetime and droplet diameter over all droplets at all times, are important subjects of future research.

Finally, in addition to the comparison of a variety of steady-state statistics seen in Chandrakar *et al.* [7], we also observe many of the same transient features which occur when abruptly stopping the aerosol injection. These were explored experimentally in Chang *et al.* [3] and Chandrakar *et al.* [6], and the rapid acceleration of cloud collapse as the interstitial aerosols are depleted is well represented in the DNS. Depending on the preceding aerosol injection rate (and therefore reservoir size), the broadening of the DSD in time near total collapse can be quite dramatic, with a low number of large droplets rapidly forming and settling out of the domain.

We conclude by stating that DNS of turbulent Rayleigh-Bénard flow is a powerful tool for understanding not only the Pi Chamber experiments but also by extension the insights into cloud microphysics which are accessible through such a setup. Processes associated with aerosol composition and size, as well as the refinement of Lagrangian properties needed by stochastic models are now possible from a new perspective and will be the subject of ongoing research.

## **ACKNOWLEDGMENTS**

This research was funded by the Office of Naval Research Award N00014-16-1-2472 and Army Research Office Award G00003613-ArmyW911NF-17-0366. Computer resources were made available through the Notre Dame Center for Research Computing and the DoD High Performance Computing Modernization Program. W.H.C. and R.A.S. were supported by National Science Foundation Grant No. AGS-1754244.

#### APPENDIX

Above, Eqs. (5)–(8) were simplified to highlight the basic structure of the droplet location, velocity, size, and temperature evolution. Here we provide the full equations, which can also be found in Richter *et al.* [31]:

$$\frac{d\mathbf{x}_p^i}{dt} = \mathbf{v}_p^i,\tag{A1}$$

$$\frac{d\mathbf{v}_{p}^{i}}{dt} = \frac{1}{\tau_{p}} (\mathbf{u}_{f} - \mathbf{v}_{p}^{i}) - g_{p} \hat{\mathbf{k}}, \tag{A2}$$

$$\frac{dd_p^i}{dt} = \frac{1}{9} \frac{\operatorname{Sh}_p}{\operatorname{Sc}} \frac{\rho_p}{\rho_w} \frac{d_p^i}{\tau_p} (q_f - q_*), \tag{A3}$$

$$\frac{dT_{p}^{i}}{dt} = -\frac{1}{3} \frac{\text{Nu}_{p}}{\text{Pr}} \frac{c_{p,a}}{c_{L}} \frac{\rho_{p}}{\rho_{w}} \frac{1}{\tau_{p}} (T_{p}^{i} - T_{f}) + 3L_{v} \frac{1}{d_{p}^{i} c_{L}} \frac{dd_{p}^{i}}{dt}, \tag{A4}$$

Symbol	Description	Value/expression	
$\overline{\nu_a}$	Kinematic viscosity of air	$1.57 \times 10^{-5} \text{ m}^2 \text{ s}^{-1}$	
$ ho_a$	Density of dry air	$1.2 \text{ kg m}^{-3}$	
$ ho_w$	Density of pure water	$1000 \text{ kg m}^{-3}$	
$ ho_p$	Density of droplet (inc. solute)	Variable	
$c_{p,a}$	Sp. heat of air at const. press.	$1006 \text{ J} (\text{kg K})^{-1}$	
$c_{p,v}$	Sp. heat of water vapor at const. press.	$1952 \text{ J} (\text{kg K})^{-1}$	
$c_L$	Specific heat of liquid water	$4179 \text{ J } (\text{kg K})^{-1}$	
$L_v$	Latent heat of vaporization	$2.44 \times 10^6 \text{ J kg}^{-1}$	
$R_d$	Gas constant of dry air	$287 \text{ J } (\text{kg K})^{-1}$	
$R_u$	Universal gas constant	$8.314 \text{ J } (\text{mol K})^{-1}$	
$M_w$	Molecular weight of water	$0.018 \; \mathrm{kg}  \mathrm{mol}^{-1}$	
$M_s$	Molecular weight of solute	$0.0584 \text{ kg mol}^{-1}$	
σ	Air-water surface tension	$7.28 \times 10^{-2} \text{ N m}^{-1}$	
Sc	Dimensionless Schmidt number	0.615	
Pr	Dimensionless Prandtl number	0.71	
$Sh_p$	Dimensionless Sherwood number	$Sh_p = 2 + 0.6 \operatorname{Re}_p^{1/2} \operatorname{Sc}^{1/3}$	
$Nu_p$	Dimensionless Nusselt number	$Nu_p = 2 + 0.6 \operatorname{Re}_p^{1/2} \operatorname{Pr}^{1/3}$	
$Re_p$	Droplet Reynolds number	$Re_p = 2r_p^i  \mathbf{v}_p^i - \mathbf{u}_f  / \nu_a$	

TABLE II. Droplet model parameters.

where, as stated above,  $\mathbf{u}_f$ ,  $q_f$ , and  $T_f$  are the air velocity, water vapor mixing ratio, and temperature interpolated to the droplet location using sixth-order Lagrange interpolation. The water vapor mixing ratio at the droplet surface,  $q_*$ , includes modifications to the water vapor pressure due to both curvature and salinity:

$$q_* = \frac{M_w}{R_u T_p^i \rho_a} e_s \exp\left[\frac{L_v M_w}{R_u} \left(\frac{1}{T_f} - \frac{1}{T_p^i}\right) + \frac{M_w \sigma}{R_u \rho_w d_p^i T_p^i} - \frac{I \Phi_s m_s^i (M_w / M_s)}{\rho_w \pi d_p^{i3} / 6}\right],\tag{A5}$$

where  $M_w$  is the molecular weight of water,  $R_u$  is the universal gas constant,  $L_v$  is the latent heat of vaporization,  $\sigma$  is the surface tension between water and air, I is the number of diassociated ions in the solute (assumed NaCl),  $\Phi_s$  is an osmotic coefficient,  $m_s^i$  is the solute mass of the particle,  $\rho_a$  is the density of air, and  $\rho_w$  is the density of pure water. The saturation vapor pressure  $e_s$  is evaluated at the local air temperature  $T_f$  according to the modified Magnus relation of Alduchov and Eskridge [41].

In addition to these parameters, Eqs. (A1)–(A5) also contain a number of material properties and nondimensional parameters which are listed in Table II. In particular, Eqs. (A3) and (A4) include the Sherwood  $(Sh_p)$  and Nusselet  $(Nu_p)$  numbers, which account for ventilation effects in droplet vapor and mass transfer from the droplet surface, as well as the Schmidt (Sc) and Prandtl (Pr) numbers, which specify the vapor and temperature diffusivities.

<sup>[1]</sup> R. A. Shaw, Particle-turbulence interactions in atmospheric clouds, Annu. Rev. Fluid Mech. **35**, 183 (2003).

<sup>[2]</sup> W. W. Grabowski and L.-P. Wang, Growth of cloud droplets in a turbulent environment, Annu. Rev. Fluid Mech. 45, 293 (2013).

<sup>[3]</sup> K. Chang, J. Bench, M. Brege, W. Cantrell, K. K. Chandrakar, D. Ciochetto, C. Mazzoleni, L. R. Mazzoleni, D. Niedermeier, and R. A. Shaw, A laboratory facility to study gas-aerosol cloud interactions in a turbulent environment: The Pi chamber, Bull. Am. Meteorol. Soc. 97, 2343 (2016).

- [4] D. Niedermeier, K. Chang, W. Cantrell, K. K. Chandrakar, D. Ciochetto, and R. A. Shaw, Observation of a link between energy dissipation rate and oscillation frequency of the large-scale circulation in dry and moist rayleigh-bénard turbulence, Phys. Rev. Fluids 3, 083501 (2018).
- [5] J. Anderson, S. Thomas, P. Prabhakaran, R. Shaw, and W. Cantrell, Effects of the large-scale circulation on temperature and water vapor distributions in the Π Chamber, Atmos. Meas. Tech. 14, 5473 (2021).
- [6] K. K. Chandrakar, W. Cantrell, D. Ciochetto, S. Karki, G. Kinney, and R. A. Shaw, Aerosol removal and cloud collapse accelerated by supersaturation fluctuations in turbulence, Geophys. Res. Lett. 44, 4359 (2017).
- [7] K. K. Chandrakar, W. Cantrell, K. Chang, D. Ciochetto, D. Niedermeier, M. Ovchinnikov, R. A. Shaw, and F. Yang, Aerosol indirect effect from turbulence-induced broadening of cloud-droplet size distributions, Proc. Natl. Acad. Sci. USA 113, 14243 (2016).
- [8] N. Desai, K. K. Chandrakar, K. Chang, W. Cantrell, and R. A. Shaw, Influence of microphysical variability on stochastic condensation in a turbulent laboratory cloud, J. Atmos. Sci. 75, 189 (2018).
- [9] K. K. Chandrakar, W. Cantrell, and R. A. Shaw, Influence of turbulent fluctuations on cloud droplet size dispersion and aerosol indirect effects, J. Atmos. Sci. 75, 3191 (2018).
- [10] A. S. M. Shawon, P. Prabhakaran, G. Kinney, R. A. Shaw, and W. Cantrell, Dependence of aerosol-droplet partitioning on turbulence in a laboratory cloud, Geophys Res Atmos 126, e2020JD033799 (2021).
- [11] P. Prabhakaran, A. S. M. Shawon, G. Kinney, S. Thomas, W. Cantrell, and R. A. Shaw, The role of turbulent fluctuations in aerosol activation and cloud formation, Proc. Natl. Acad. Sci. USA 117, 16831 (2020).
- [12] N. Desai, K. Chandrakar, G. Kinney, W. Cantrell, and R. Shaw, Aerosol-mediated glaciation of mixedphase clouds: Steady-state laboratory measurements, Geophys. Res. Lett. 46, 9154 (2019).
- [13] C. D. Packard, M. L. Larsen, S. Thomas, W. H. Cantrell, and R. A. Shaw, Light scattering in a turbulent cloud: Simulations to explore cloud-chamber experiments, Atmosphere 11, 837 (2020).
- [14] R. Paoli and K. Shariff, Turbulent condensation of droplets: Direct simulation and a stochastic model, J. Atmos. Sci. 66, 723 (2009).
- [15] G. Sardina, F. Picano, L. Brandt, and R. Caballero, Continuous Growth of Droplet Size Variance Due to Condensation in Turbulent Clouds, Phys. Rev. Lett. 115, 184501 (2015).
- [16] C. Siewert, J. Bec, and G. Krstulovic, Statistical steady state in turbulent droplet condensation, J. Fluid Mech. 810, 254 (2017).
- [17] W. A. Cooper, Effects of variable droplet growth histories on droplet size distributions. Part I: Theory, J. Atmos. Sci. 46, 1301 (1989).
- [18] P. A. Vaillancourt, M. K. Yau, and W. W. Grabowski, Microscopic approach to cloud droplet growth by condensation. Part I: Model description and results without turbulence, J. Atmos. Sci. 58, 1945 (2001).
- [19] P. A. Vaillancourt, M. K. Yau, P. Bartello, and W. W. Grabowski, Microscopic approach to cloud droplet growth by condensation. Part II: Turbulence, clustering, and condensational growth, J. Atmos. Sci. 59, 3421 (2002).
- [20] B. Kumar, J. Schumacher, and R. A. Shaw, Cloud microphysical effects of turbulent mixing and entrainment, Theor. Comput. Fluid Dyn. 27, 361 (2013).
- [21] P. Götzfried, B. Kumar, R. A. Shaw, and J. Schumacher, Droplet dynamics and fine-scale structure in a shearless turbulent mixing layer with phase changes, J. Fluid Mech. 814, 452 (2017).
- [22] S. Thomas, M. Ovchinnikov, F. Yang, D. van der Voort, W. Cantrell, S. K. Krueger, and R. A. Shaw, Scaling of an atmospheric model to simulate turbulence and cloud microphysics in the Pi Chamber, J. Adv. Model. Earth Syst. 11, 1981 (2019).
- [23] W. W. Grabowski, Comparison of Eulerian bin and Lagrangian particle-based schemes in simulations of Pi chamber dynamics and microphysics, J. Atmos. Sci. 77, 1151 (2019).
- [24] I. Saito, T. Gotoh, and T. Watanabe, Broadening of cloud droplet size distributions by condensation in turbulence, J. Meteorol. Soc. Jpn. **97**, 867 (2019).
- [25] L. Thomas, W. W. Grabowski, and B. Kumar, Diffusional growth of cloud droplets in homogeneous isotropic turbulence: DNS, scaled-up DNS, and stochastic model, Atmos. Chem. Phys. **20**, 9087 (2020).
- [26] S. K. Krueger, Technical note: Equilibrium droplet size distributions in a turbulent cloud chamber with uniform supersaturation, Atmos. Chem. Phys. **20**, 7895 (2020).

- [27] J. P. Mellado, C. S. Bretherton, B. Stevens, and M. C. Wyant, DNS and LES for simulating stratocumulus: Better together, J. Adv. Model. Earth Syst. 10, 1421 (2018).
- [28] M. Andrejczuk, J. M. Reisner, B. Henson, M. K. Dubey, and C. A. Jeffery, The potential impacts of pollution on a nondrizzling stratus deck: Does aerosol number matter more than type?, J. Geophys. Res. 113, D19204 (2008).
- [29] S. Shima, K. Kusano, A. Kawano, T. Sugiyama, and S. Kawahara, The super-droplet method for the numerical simulation of clouds and precipitation: A particle-based and probabilistic microphysics model coupled with a non-hydrostatic model, Q.J.R. Meteorol. Soc. 135, 1307 (2009).
- [30] T. Riechelmann, Y. Noh, and S. Raasch, A new method for large-eddy simulations of clouds with Lagrangian droplets including the effects of turbulent collision, New J. Phys. 14, 065008 (2012).
- [31] D. H. Richter, T. MacMillan, and C. Wainwright, A Lagrangian cloud model for the study of marine fog, Bound.-Layer Meteorol. **181**, 523 (2021).
- [32] H. J. Park, K. O'Keefe, and D. H. Richter, Rayleigh-Bénard turbulence modified by two-way coupled inertial, nonisothermal particles, Phys. Rev. Fluids 3, 034307 (2018).
- [33] B. Helgans and D. H. Richter, Turbulent latent and sensible heat flux in the presence of evaporative droplets, Int. J. Multiphase Flow 78, 1 (2016).
- [34] G. I. Barenblatt, A. J. Chorin, and V. M. Prostokishin, A note concerning the Lighthill "sandwich model" of tropical cyclones., Proc. Natl. Acad. Sci. USA 102, 11148 (2005).
- [35] W. Grabowski and L. Thomas, Cloud droplet diffusional growth in homogeneous isotropic turbulence: Bin microphysics versus Lagrangian superdroplet simulations, Atmos. Chem. Phys. 21, 4059 (2021).
- [36] O. Shishkina, R. J. A. M. Stevens, S. Grossmann, and D. Lohse, Boundary layer structure in turbulent thermal convection and its consequences for the required numerical resolution, New J. Phys. 12, 075022 (2010).
- [37] K. K. Chandrakar, W. Cantrell, S. Krueger, R. A. Shaw, and S. Wunsch, Supersaturation fluctuations in moist turbulent Rayleigh-Bénard convection: A two-scalar transport problem, J. Fluid Mech. 884, A19 (2020).
- [38] S. Thomas, P. Prabhakaran, W. Cantrell, and R. A. Shaw, Is the water vapor supersaturation distribution Gaussian? J. Atmospheric Sci. 78, 2385 (2021).
- [39] W. A. Hoppel, G. M. Frick, and R. E. Larson, Effect of nonprecipitating clouds on the aerosol size distribution in the marine boundary layer, Geophys. Res. Lett. 13, 125 (1986).
- [40] F. Yang, P. Kollias, R. A. Shaw, and A. M. Vogelmann, Cloud droplet size distribution broadening during diffusional growth: Ripening amplified by deactivation and reactivation, Atmos. Chem. Phys. 18, 7313 (2018).
- [41] O. A. Alduchov and R. E. Eskridge, Improved Magnus form approximation of saturation vapor pressure, J. Appl. Meteor. **35**, 601 (1996).